Numerical investigation of forced convective MHD tangent hyperbolic nanofluid flow with heat source/sink across a permeable wedge

Cite as: AIP Advances 14, 065302 (2024); doi: 10.1063/5.0196862
Submitted: 10 January 2024 • Accepted: 10 May 2024 •
Published Online: 3 June 2024

Taghreed A. Assiri,[1] Muhammad Bilal,[2,a)] Emad E. Mahmoud,[3] Aatif Ali,[4] Joshua Kiddy K. Asamoah,[5,6,a)] and Adnan[7]

AFFILIATIONS

[1] Mathemtaics Department, Faculty of Sciences, Umm Al-Qura University, Makkah, Saudi Arabia
[2] Sheikh Taimur Academic Block-II, Department of Mathematics, University of Peshawar, 25120 Khyber Pakhtunkhwa, Pakistan
[3] Department of Mathematics and Statistics, Collage of Science, Taif University, P.O. Box 11099, Taif 21944, Saudi Arabia
[4] School of Mathematical Sciences, Jiangsu University, Zhenjiang, Jiangsu 212013, China
[5] Department of Mathematics, Saveetha School of Engineering SIMATS, Chennai, India
[6] Department of Mathematics, Kwame Nkrumah University of Science and Technology, Kumasi, Ghana
[7] Department of Mathematics, Mohi-ud-Din Islamic University, Nerian Sharif, AJ&K 12080, Pakistan

[a)] **Authors to whom correspondence should be addressed:** bilalchd345@gmail.com and jkkasamoah@knust.edu.gh

ABSTRACT

The combined effect of wedge angle and melting energy transfer on the tangent hyperbolic magnetohydrodynamics nanofluid flow across a permeable wedge is numerically evaluated. Electronic gadgets produce an excessive amount of heat while in operation, so tangent hyperbolic nanofluid (THNF) is frequently used to cool them. THNF has the potential to dissipate heat more efficiently, thereby lowering the possibility of excessive heat and malfunctioning components. The effects of thermal radiation and heat source/sink are also examined on the flow of THNF. The flow has been formulated in the form of PDEs, which are numerically computed through the MATLAB solver BVP4c. The numerical results of BVP4c are relatively compared to the published work for validity purposes. It has been detected that the results are accurate and reliable. Furthermore, from the graphical results, it has been perceived that the rising impact of the Weissenberg number accelerates the velocity and thermal profile. The effect of the power-law index parameter drops the fluid temperature, but enhances the velocity curve. The variation in the wedge angle boosts the shearing stress and energy propagation rate, whereas the increment of Wi declines both the energy transfer rate and skin friction.

NOMENCLATURE

A	second-order tensor
$B(x)$	variable magnetic field
B_0	magnetic field constant
C	concentration
C_∞	ambient concentration
C_f	skin friction
C_s	heat capacity
C_w	wall concentration
D_4	Dufour number
D_B	Brownian diffusion
D_T	thermophoresis diffusion
f'	non-dimensional velocity
k	thermal conductivity
K'	permeability constant
K_c	chemical reaction
K_p	medium permeability
k_T	fluid thermal diffusion ratio
$K(x)$	variable permeability

Le	Lewis number
M	magnetic field
m	wedge angle parameter
n	power law index
Pr	Prandtl number
Q_e	heat source/sink factor
Q_e^*	exponential heat source/sink
Rd	thermal radiation
Re_x	local Reynolds number
Sr	Soret number
T	fluid temperature
T_0	surface temperature
T_∞	ambient temperature
T_m	surface temperature due to melting
$U(x)$	velocity of boundary layer
Wi	Weissenberg number
α	thermal diffusivity
β_1	Hartree pressure gradient
η	similarity variable
θ	dimensionless temperature
κ^*	absorption constant
$\psi(x,y)$	stream function
Λ	heat capacity
λ	nanofluid latent heat
ρ	density
σ	electrical conductivity
$\sigma*$	Stefan–Boltzmann constant
υ	fluid viscosity
ϕ	dimensionless concentration
Ω	wedge angle

I. INTRODUCTION

Automobiles, the creation of steam-electric power, heating and air conditioning, the cooling of electronic devices energy systems, and disease diagnosis are just a few of the industrial applications of heat transference. Transfer of heat is the kinetic phenomenon that can be analyzed and investigated independently or in combination. It is easier to study diffusion and convection separately, although in both cases, the fundamental physical processes can be characterized by the same set of mathematical equations. Some processes, such as evaporative cooling and burning, require simultaneous consideration of heat transmission. The integration of heat assignment phenomena plays a significant role in several industrial processes, particularly in recent years. Examples of such processes include drying operations, evaporation on water surfaces, energy recovering procedures, and chemical sector applications. Heat and mass transmissions occur simultaneously; for example, in the power sector, the extraction of kinetic energy from a fluid in motion is a common method of power generation. Mass transfer and heat transfer find extensive utilization in several industrial contexts, including welding, magma solidification, casting processes, defrost of frozen ground, and the melting of permafrost.[1] Processing of polymers, ground water pollution, nuclear power plants, geothermal industry, modeling of warships, packed bed reactors, and other processes are some examples of applications for such flow.[2] The consequence of viscous dissipation nanoparticle volume fraction, thermal radiation, wedge angle parameter, and heat absorption/generation on the Sisko fluid flow having dispersed nanomaterials across a wedge plate was inspected by Dadhich *et al.*[3] According to the findings, thermal transfer declines with rising magnetic field and Eckert number, but the mass transfer rate increases with the increasing pressure gradient parameter. Tassaddiq *et al.*,[4] Alharbi *et al.*,[5] and Alharbi *et al.*[6] estimated the nanoliquid flow along a shrinking/stretching surface with energy and mass transfer. Incorporating nonlinear thermal characteristics, Assiri *et al.*[7] and Rahman *et al.*[8] assessed the fluid flow across a wedge and some solutions of optical solitary wave solution. The outcome shows that as the temperature ratio parameter increases, temperature profiles increase, while the concentration boundary layer thickness decreases. The dissipative effect on the Jeffrey fluid over a wedge was analyzed by Dharmaiah *et al.*[9] Butt *et al.*[10] employed an innovative model of inversely multiquadric radial-based artificial neural networks to assess the magnetized nanoliquid flow across a wedge. Rana *et al.*[11] elaborated the heat transit characteristics of 3D nanoliquid flow composed of multi-walled carbon nanotube (MWCNT) and MgO dispersed in EG across a wedge.

Non-Newtonian fluids exhibit a diverse range of kinds, each possessing distinct features. In comparison with other kinds of non-Newtonian fluids, the tangent hyperbolic nanofluid (THNF) mathematical model possesses numerous notable advantages. Numerous researchers from all over the world have recently examined tangent hyperbolic fluids in depth.[12] Kebede *et al.*[13] calculated the unsteady THNF flow over a penetrable wedge. Shahzad *et al.*[14] examined the two-dimensional unsteady THNF flow under the upshot of suction-injection. Using motile gyrotactic microbes and unsteady THNF, Hussain *et al.*[15] deliberated the impact of magnetohydrodynamics (MHD) and porosity on the fluid flow over a wedge with second-order slip. Ud Din *et al.*[16] inspected the thermal transport through THNF flow over a wedge with gyrotactic micro-organisms. The implications of activation energy on the gyrotactic micro-organisms THNF flow across slender sheet were inspected by Yahya *et al.*[17] and Alharbi *et al.*[18] The thermophysical effects of THNF flow over a movable wedge were investigated by Mahdy and Chamkha.[19] Weissenberg numbers with larger values are associated with improved skin friction coefficients, as demonstrated by the results.

There are several chemical, mechanical, and industrial applications that rely significantly on chemical conversions. In order to control the rate of a chemical reaction (CR), a considerable quantity of oxygen that can be converted into activation energy (AE) is necessary. The energy needed to initiate a chemical reaction is often referred to as AE. Svante Arrhenius in 1889 proposed the fundamental concept of AE.[20] Waqas *et al.*[21] estimated the fluid flow with activation energy across a shrinking/stretching wedge. An unsteady non-Newtonian nanofluid's MHD Falkner–Skan wedge flow with activation energy was reported by Ali *et al.*[22] Bilal *et al.*[23] numerically analyzed the unsteady flow of MHD nanoliquids over a slender Riga sheet subject to activation energy. Over a spinning disk, Alsallami *et al.*[24] used numerical simulations to examine the entropy anatomization of the Marangoni Maxwell nanofluid flow. With the existence of Cattaneo–Christov double diffusion, thermal radiation, endothermic/exothermic reactions, and thermal conductivity, Sajid *et al.*[25] surveyed the effects of a modified Buongiorno ternary hybrid nanoliquid flow over wedge. The nanofluid boundary layer flow,

including gyrotactic microbes with AE and buoyancy force, was numerically assessed by Othman *et al.*[26]

Heat sources and sinks are commonly employed in order to maintain optimal cooling conditions for electronic devices. The utilization of heat source and sink effects possesses a diverse array of applications in several domains, such as recovering of crude oil, the execution of radial diffusers, and the refrigeration of metallic sheets. Ramzan *et al.*[27] examined the dusty flow Casson nanofluid in a magnetohydrodynamic (MHD) fluid with a varying heat source and Fick's and Fourier's laws across a stretchable pipe. Using a modified Buongiorno model, Mahanthesh *et al.*[28] scrutinized the impact of an irregular partial heat slip, source/sink, and Newton boundary conditions on the convective flow of fluid across an extending surface. Adnan *et al.*[29] studied the nanoliquid flow through a cylinder with the upshot of heat source/sink and mixed convective. Sharma and Gandhi[30] investigated the joined impact of MHD and heat source–sink on a Darcy–Forchheimer flow across a vertical extending porous medium. The impact of nonlinear heat source/sink on the radiative ternary convective nanoliquid was numerically studied by Adnan *et al.*[31] Gul *et al.*[32] considered the MHD viscous dissipated nanoliquid flow with forced convection and heat source.

From the above literature, it has been decided that so far no one has elaborated the tangent hyperbolic MHD nanoliquid flow across a permeable wedge with the consequences of CR and heat source/sink. Therefore, we have estimated numerically the combined effect of wedge angle and melting energy transfer on the tangent hyperbolic MHD nanoliquid flow across a permeable wedge with the significances of Soret and Dufour and thermal radiation. The THNF flow has been formulated in the form of PDEs, which are numerically computed through the BVP4c. The numerical results of BVP4c are compared to the published work for the validity purpose. The core novelties of the proposed model are as follows:

- To study the tangent hyperbolic MHD nanofluid flow across a permeable vertical wedge.
- To elaborate the consequences of magnetic field and buoyancy forces.
- To examine the energy transfer under the significances of exponential heat source/sink and thermal radiation.
- To assess the mass diffusion over a permeable surface subject to Arrhenius AE and second-order CR.
- To derive the numerical solution of nonlinear system of coupled PDEs.

In Sec. II, the problem is formulated and physically described.

II. MATHEMATICAL FORMULATION

In this article, in the presence of diffusion-thermo, melting heat transfer, and thermo-diffusion, a two-dimensional unsteady forced convective, electrically conducting, radiating, incompressible flow of THNF over a porous wedge is inspected. C_w denotes the wall concentration, and T_m represents the surface temperature due to the melting process. $U(x) = ax^m$ is supposed to be the velocity of nanofluid above the boundary layer. Here, a is a positive constant. The variable magnetic field is applied perpendicular to the wedge's surface as $B(x) = B_0 x^{\left(\frac{m-1}{2}\right)}$. The surface permeability is stated in as $K(x) = K' x^{-(m-1)}$. $m = \frac{\beta_1}{2-\beta_1}$ is the wedge angle factor, where β_1 signifies the Hartree pressure gradient. T_∞ is the temperature of the nanofluid away from the surface. Here, $T_\infty < T_m$ as well as $T_0 < T_m$. The physical sketch of the fluid flow is shown in Fig. 1. The following form can be used to express the hyperbolic tangential fluid equation's constitutive representation:

$$\tau = \left[(\mu_\infty + \mu_0)\tanh\left(\Gamma\dot{\Omega}\right)^n + \mu_\infty\right]\dot{\Omega}. \tag{1}$$

Here, τ and Γ are the extra stress tensor and material constant, where $\dot{\Omega}$ can be formulated as

$$\dot{\Omega} = \sqrt{\frac{\sum_k \sum_m \dot{\Omega}_{km}\dot{\Omega}_{mk}}{2}} = \sqrt{\frac{A}{2}}. \tag{2}$$

The aforementioned statement denotes that the symbol A represents the invariant of the second-order strain rate tensor. The term can be specified as

$$A = \frac{tr\left(L^T + L\right)^2}{2}, \tag{3}$$

where $L = (gradV)$, in which $\mathbf{V}$ signifies the velocity of the fluid. Assume that $\mu_\infty = 0$ and that we are concentrating on the THNF, which indicates a shear thinning behavior when $\Gamma\dot{\Omega} < 1$, and the expression τ reduces to

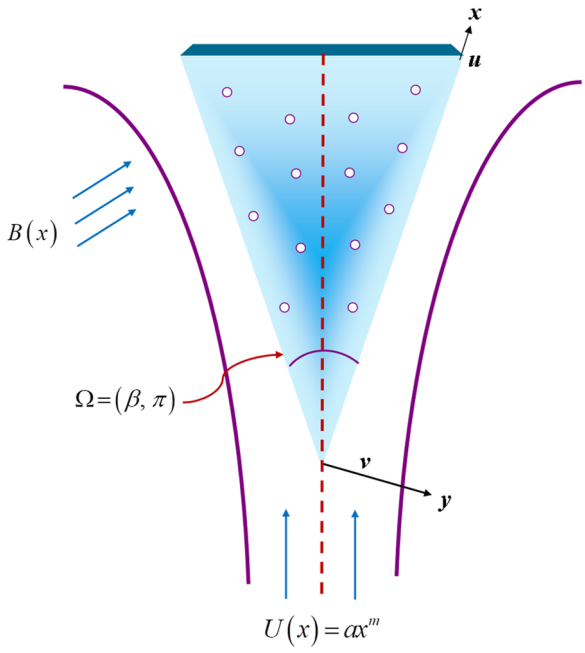

FIG. 1. Physical geometry of the fluid flow.

$$\begin{aligned}\tau &= \mu_0\dot{\Omega}\left[\left(\Gamma\dot{\Omega}\right)^n\right]\\ &= \mu_0\dot{\Omega}\left[\left(-1+1+\Gamma\dot{\Omega}\right)^n\right]\\ &= \mu_0\dot{\Omega}\left[-1+n\left(\Gamma\dot{\Omega}+1\right)\right].\end{aligned} \tag{4}$$

The governing equations for the THNF flow can be stated as follows:[33–35]

$$\frac{\partial u}{\partial x}+\frac{\partial v}{\partial y}=0, \tag{5}$$

$$\begin{aligned}u\left(\frac{\partial u}{\partial x}\right)+v\left(\frac{\partial u}{\partial y}\right) &= U(x)\left(\frac{\partial U(x)}{\partial x}\right)+\left(\frac{\sigma B^2(x)}{\rho_f}+\frac{\upsilon}{K(x)}\right)\\ &\times\left(U(x)-u\right)+\upsilon\left[\left(\sqrt{2}\Gamma\left(\frac{\partial u}{\partial y}\right)-1\right)n+1\right]\\ &\times\frac{\partial^2 u}{\partial y^2}+g\beta_T(T-T_\infty)\cos\gamma\\ &+g\beta_C(C-C_\infty)\cos\gamma,\end{aligned} \tag{6}$$

$$\begin{aligned}u\left(\frac{\partial T}{\partial x}\right)+v\left(\frac{\partial T}{\partial y}\right)&\\ =\alpha\frac{\partial^2 T}{\partial y^2}+\frac{\kappa_T D_B}{C_s C_p}\frac{\partial^2 C}{\partial y^2}+\Lambda&\left\{D_B\frac{\partial C}{\partial y}\frac{\partial T}{\partial y}+\frac{D_T}{T_\infty}\left(\frac{\partial T}{\partial y}\right)^2\right\}\\ -\frac{1}{\rho C_p}\frac{\partial q_r}{\partial y}+\frac{Q_e^*}{(\rho C_p)_{hnf}}&+(T-T_\infty)\exp\left(-\sqrt{\frac{a}{\upsilon_f}}ny\right),\end{aligned} \tag{7}$$

$$\begin{aligned}u\left(\frac{\partial C}{\partial x}\right)+v\left(\frac{\partial C}{\partial y}\right)&=\frac{\kappa_T D_B}{T_m}\frac{\partial^2 T}{\partial y^2}+\frac{D_T}{T_\infty}\frac{\partial^2 T}{\partial y^2}+D_B\frac{\partial^2 C}{\partial y^2}\\ &-K_r^2\left(\frac{T}{T_\infty}\right)^n\exp\left(\frac{-E_a}{\kappa T}\right)(C-C_\infty).\end{aligned} \tag{8}$$

Here, (u,v) represent the velocity terms, Q_e^* is the exponential heat source/sink term, D_B specifies the Brownian diffusion, K_r presents the rate of chemical reaction, D_T is the thermophoresis diffusion, k_T characterizes the fluid thermal diffusion ratio, $\Lambda=\frac{(\rho c)_p}{(\rho c)_f}$ describes the heat capacity of the nanofluid, $\alpha=\frac{k}{(\rho c)_f}$ signifies the nanofluid thermal diffusivity, E_a is the activation energy term, υ denotes the fluid viscosity, σ denotes the fluid electrical conductivity, and n represents the fluid power law index.

The boundary conditions (BCs) are

$$\left.\begin{aligned}T=T_m,\quad u=0,\quad v=0,\quad k\frac{\partial T}{\partial y}=\rho v(x,0)\left(C_s(T_m-T_0)+\lambda\right),\quad C=C_w\quad\text{at}\quad y=0,\\ u\to U(x),\quad v=0,\quad C\to C,\quad T\to T_\infty\quad\text{as}\quad y\to\infty.\end{aligned}\right\} \tag{9}$$

Here, λ indicates the nanofluid latent heat, k indicates the nanofluid thermal conductivity, T_0 represents the solid surface temperature of the nanofluid, C_s indicates the nanofluid heat capacity of the solid surface, and ρ indicates the nanofluid density.

The term q_r is expressed as

$$q_r=-\frac{4\sigma^*}{\kappa^*}\frac{\partial T^4}{\partial y} \tag{10}$$

and

$$T^4\cong -3T_\infty^4+4T_\infty^3 T, \tag{11}$$

where κ^* is the absorption constant, while $\sigma*$ symbolizes the Stefan–Boltzmann constant.

Placing Eqs. (10) and (11) in (7) yields

$$\begin{aligned}u\left(\frac{\partial T}{\partial x}\right)+v\left(\frac{\partial T}{\partial y}\right)&=\left(\alpha+\frac{16\alpha^* T_\infty^2}{3\rho C_p\kappa^*}\right)\frac{\partial^2 T}{\partial y^2}+\frac{\kappa_T D_B}{C_S C_P}\frac{\partial^2 C}{\partial y^2}\\ &+\Lambda\left\{D_B\frac{\partial C}{\partial y}\frac{\partial T}{\partial y}+\frac{D_T}{T_\infty}\left(\frac{\partial T}{\partial y}\right)^2\right\}\\ &+\frac{Q_e^*}{(\rho C_p)_{hnf}}+(T-T_\infty)\exp\left(-\sqrt{\frac{a}{\upsilon_f}}ny\right).\end{aligned} \tag{12}$$

The stream function $\psi(x,y)$ is stated as

$$\frac{\partial\psi}{\partial y}=u,\qquad \frac{\partial\psi}{\partial x}=-v. \tag{13}$$

The similarity variables are

$$\begin{aligned}\eta&=\left(\frac{(m+1)U(x)}{2x\upsilon}\right)^{\frac{1}{2}}y,\qquad T=\theta(\eta)(T_m-T_\infty)+T_\infty,\\ \psi&=\left(\frac{2\upsilon x U(x)}{m+1}\right)^{\frac{1}{2}}f(\eta),\qquad \frac{C-C_\infty}{(C_w-C_\infty)}=\phi(\eta).\end{aligned} \tag{14}$$

By employing Eq. (14) into a set of PDEs, we get

$$\left(1-n\left(1-Wif''\right)\right)f''' + \frac{2m\left(1-f'^2\right)}{1+m} + \frac{\left(1-f'\right)}{K_p} + ff'' + M\left(1-f'\right) + (Gr)\theta\cos\gamma + (Gm)\phi\cos\gamma = 0, \tag{15}$$

$$\left(1+\frac{4Rd}{3}\right)\theta'' + \Pr\left\{D_4\phi'' + Nb\phi'\theta' + Nt\theta'^2 + f\theta'\right\} + Q_e\exp(-n\eta) = 0, \tag{16}$$

$$\phi'' + \Pr Le\phi' f + \theta''\left(\Pr LeSr + \frac{Nt}{Nb}\right) - C_r(\theta\Delta+1)^n\phi e^{\frac{-A_e}{(1+\Delta\theta)}} = 0. \tag{17}$$

The transformed BCs are

$$\left.\begin{aligned} f'(\eta)=0,\quad \theta(\eta)=1,\quad B\theta'(\eta)+\Pr f(\eta)=0,\quad \phi(\eta)=1\quad \text{at}\quad \eta=0,\\ f'(\eta)\to 1,\quad \theta(\eta)\to 0,\quad \phi(\eta)\to 0\quad \text{as}\quad \eta\to\infty. \end{aligned}\right\} \tag{18}$$

The dimensional parameters are

$$\left.\begin{aligned} K_p=\frac{aK'(m+1)}{2\nu},\quad \Pr=\frac{\nu}{\alpha},\quad B=\frac{C_f(T_m-T_0)}{\lambda+C_s(T_m-T_0)},\quad M=\frac{2\sigma B_0^2}{\rho_f a(m+1)},\quad Wi=\sqrt{\frac{U^3(x)(m+1)\Gamma^2}{x}},\\ Q_e=\frac{Q_e^*}{a(\rho C_p)_f}, Nt=\frac{D_T(T_m-T_\infty)\Lambda}{\nu T_\infty},\quad Nb=\frac{D_B(C_w-C_\infty)\Lambda}{\nu},\quad Le=\frac{\alpha}{D_B},\quad D_4=\frac{\kappa_T D_B(C_w-C_\infty)}{C_s C_p(T_m-T_\infty)},\\ Sr=\frac{\kappa_T D_B(T_m-T_\infty)}{T_m\nu(C_w-C_\infty)},\quad Rd=\frac{4\sigma^* T_\infty^3}{\kappa^*\kappa},\quad Gr=\frac{l^2 g\beta_T(T_m-T_\infty)}{\upsilon u_w},\quad Gm=\frac{l^2 g\beta_c(C_w-C_\infty)}{\upsilon u_w},\quad A_e=\frac{-E_a}{\kappa T}, \end{aligned}\right\} \tag{19}$$

where θ is the dimensionless form of temperature; f' represents the non-dimensional velocity; ϕ is the dimensionless form of concentration; Le represents the Lewis number; Pr, Nb, and Wi are the Prandtl number, Brownian diffusion, and Weissenberg number, respectively; Nt represents the thermophoresis factor; Sr represents the Soret number; D_4 represents the Dufour number; C_r is the second-order chemical reaction; M represents the magnetic field; Gr and Gm are the thermal and mass Grashof numbers, respectively; K_p represents the permeability of the medium; A_e is the activation energy factor; Rd is thermal radiation; and Q_e represents the heat source/sink factor.

The mathematical expression of melting is $B=\frac{C_p f(T_m-T_\infty)}{\lambda+C_s(T_m-T_0)}$. $\frac{C_p f(T_m-T_0)}{\lambda}$ signifies the Stefan number (liquid), and $\frac{C_s(T_m-T_0)}{\lambda}$ signifies the Stefan number for solid states. The physical quantities are expressed as

$$\left.\begin{aligned} \sqrt{Re_x}C_f=\frac{nWi}{2}\left(f''(0)\right)^2+(1-n)f''(0),\\ \frac{Nu}{\sqrt{Re_x}}=-\left(1+Rd\frac{4}{3}\right)\theta'(0),\qquad \frac{Sh}{\sqrt{Re_x}}=-\phi'(0), \end{aligned}\right\} \tag{20}$$

where Re_x is the Reynolds number.

III. NUMERICAL SOLUTION

The MATLAB boundary value problem solver BVP4c is built around the finite difference approach. In the proposed model, BVP4c is employed to numerically solve the non-dimensional system of ordinary differential equations (ODEs). For the purpose, the system of ODEs is further simplified into lowest order by using the following procedure:[36–38]

$$\left.\begin{aligned} \delta_1=f(\eta),\quad \delta_2=f'(\eta),\quad \delta_3=f''(\eta),\quad \delta_4=\theta(\eta),\\ \delta_5=\theta'(\eta),\quad \delta_6=\phi(\eta),\quad \delta_7=\phi'(\eta). \end{aligned}\right\} \tag{21}$$

By inserting Eq. (21) in Eqs. (15)–(18), the system of ODEs becomes

$$\left(1-n(1-Wi\delta_3)\right)\delta_3' + \frac{2m\left(1-\delta_2^2\right)}{1+m} + \frac{(1-\delta_2)}{K_p} + \delta_1\delta_3 + M(1-\delta_2) + (Gr)\delta_4\cos\gamma + (Gm)\delta_6\cos\gamma = 0, \tag{22}$$

$$\left(1+\frac{4Rd}{3}\right)\delta_5' + \Pr\left\{D_4\delta'_7 + Nb\delta_7\delta_5 + Nt\delta_5^2 + \delta_1\delta_5\right\} + Q_e\exp(-n\eta) = 0, \tag{23}$$

$$\delta_7' + \Pr Le\delta_7\delta_1 + \delta_5'\left(\Pr LeSr + \frac{Nt}{Nb}\right) - C_r(\delta_4\Delta+1)^n\delta_6 e^{\frac{-A_e}{(1+\Delta\theta)}} = 0. \tag{24}$$

The transmuted BCs are

$$\left.\begin{aligned} \delta_2(\eta)=0,\quad \delta_4(\eta)=1,\quad B\delta_5(\eta)+\Pr\delta_1(\eta)=0,\quad \delta_6(\eta)=1\quad \text{at}\quad \eta=0,\\ \delta_2(\eta)\to 1,\quad \delta_4(\eta)\to 0,\quad \delta_6(\eta)\to 0\quad \text{as}\quad \eta\to\infty. \end{aligned}\right\} \tag{25}$$

TABLE I. Relative comparison with the published studies.

Le	*m*	*B*	Sarkar and Endalew[38]	Endalew and Sarkar[39]	Present work
1.0	0.5	1.0	1.748 73	1.748 74	1.748 743 2
1.0	0.6	1.0	1.774 12	1.774 13	1.774 134 2
2.0	0.5	1.0	1.750 51	1.750 51	1.750 519 8
3.0	0.5	1.0	1.751 33	1.751 33	1.751 342 1
1.0	0.5	2.0	1.661 48	1.661 48	1.661 490 1
1.0	0.5	3.0	1.605 35	1.605 35	1.605 379 8

For the validity of the results of Eqs. (22)–(24), Table I is made.

IV. RESULTS AND DISCUSSION

The mutual consequences of wedge angle and melting energy transfer on the THNF flow across a permeable wedge are numerically analyzed. The modeled equations are simulated numerically via BVP4c. The core observation obtained from the BVP4c is analyzed as follows:

Figures 2–6 highlight the consequences of surface permeability K_p, n, magnetic factor M, wedge angle factor m, and Weissenberg number Wi on the velocity curve $f'(\eta)$, respectively. Figure 2 exposes that the impact of surface permeability factor K_p drops the fluid velocity. Physically, K_p is a property of permeable surface that allows fluid particles to flow through the sheet or surface. However, this effect resists the flow, which causes a lessening in the velocity outline. Figures 3 and 4 exhibit that the flow velocity $f'(\eta)$ enhances with the increment of power law index n and magnetic factor M. Physically, the Lorentz force produces due to the magnetic effect, which is also recognized as a resistive force that declines the fluid velocity $f'(\eta)$ as shown in Fig. 4. Figures 5 and 6 illustrate that the fluid velocity boosts with the impact of wedge angle term m, but diminishes against the variation in Weissenberg number Wi. In this case, increasing the wedge angle factor results in improved forced convection. In addition, this increases the velocity of the nanoliquid. Consequently, as the wedge angle factor upsurges, the speed of a THNF rises (Fig. 5). From a physical perspective, Wi is the ratio between elasticity and fluid viscosity. This physical fact explains

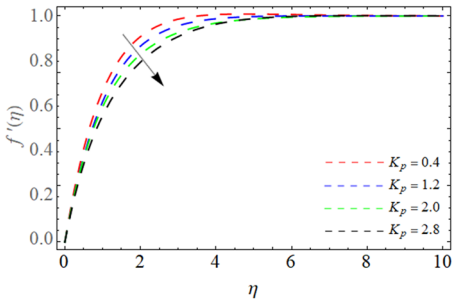

FIG. 2. Surface permeability K_p vs $f'(\eta)$.

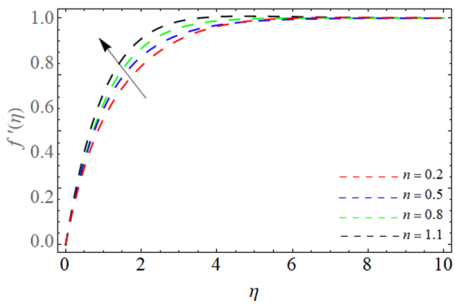

FIG. 3. Power law index n vs $f'(\eta)$.

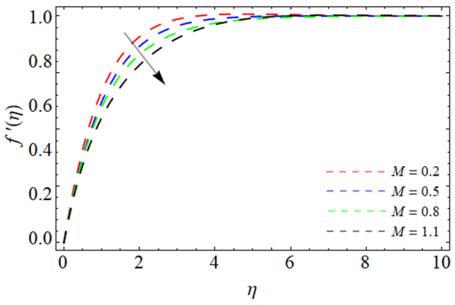

FIG. 4. Magnetic factor M vs $f'(\eta)$.

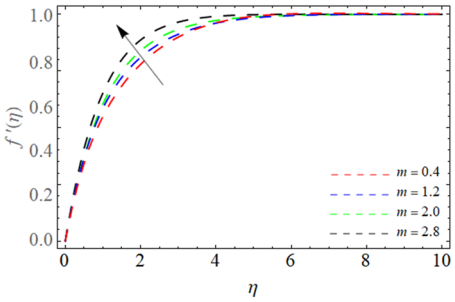

FIG. 5. Wedge angle parameter m vs $f'(\eta)$.

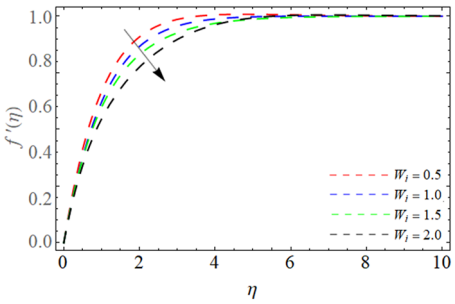

FIG. 6. Weissenberg number Wi vs $f'(\eta)$.

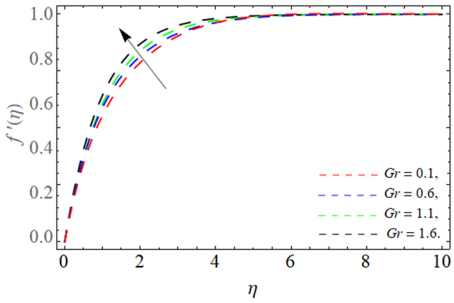

FIG. 7. Thermal Grashof *Gr* vs $f'(\eta)$.

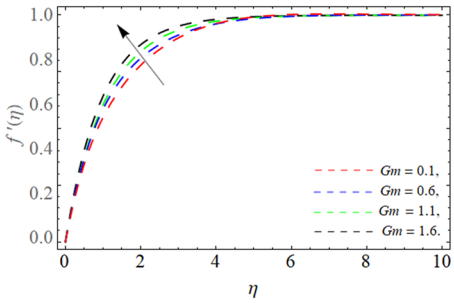

FIG. 8. Mass Grashof number *Gm* vs $f'(\eta)$.

why the thicknesses of the velocity boundary layers increase as *Wi* increases since high Weissenberg fluids have low resistivity and take more time to reach free stream velocity (Fig. 6). Figures 7 and 8 evaluate the nature of thermal *Gr* and mass Grashof number *Gm* vs $f'(\eta)$. The fluid velocity enriches with the rising impact of Grashof numbers due to the generation of buoyancy forces. The increasing effect of thermal and mass Grashof numbers usually results in elevated fluid velocity. The fluid motion intensifies as these Grashof numbers increase because buoyancy forces become more effective.

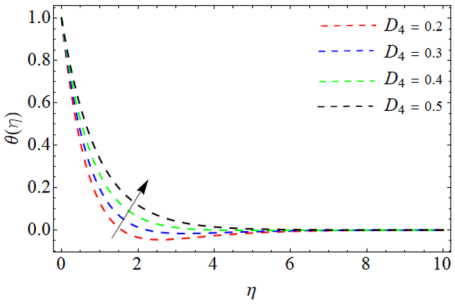

FIG. 9. Dufour number D_4 vs $\theta(\eta)$.

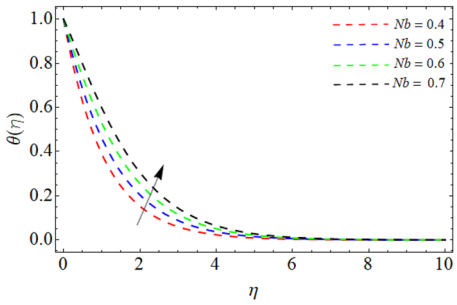

FIG. 10. Brownian motion *Nb* vs $\theta(\eta)$.

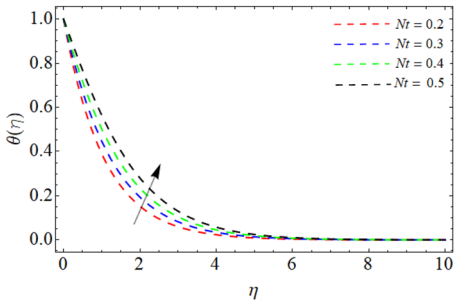

FIG. 11. Thermophoresis factor *Nt* vs $\theta(\eta)$.

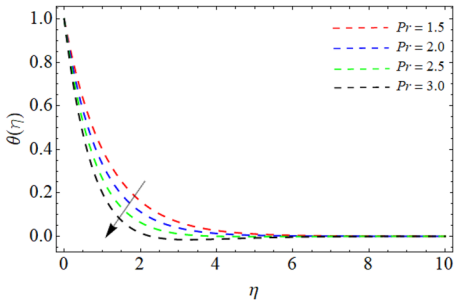

FIG. 12. Prandtl number *Pr* vs $\theta(\eta)$.

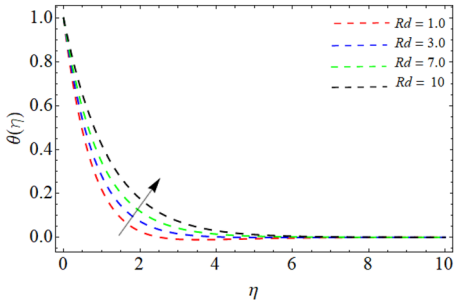

FIG. 13. Thermal radiation factor *Rd* vs $\theta(\eta)$.

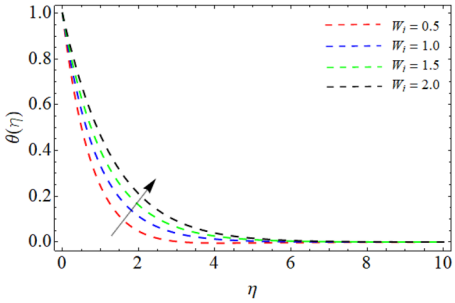

FIG. 14. Weissenberg number *Wi* vs $\theta(\eta)$.

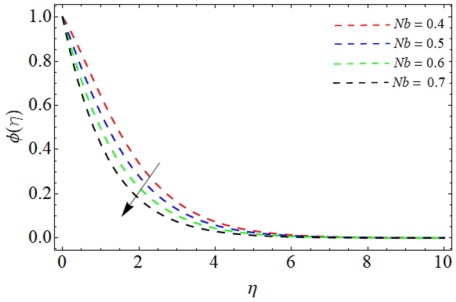

FIG. 15. Brownian motion *Nb* vs $\phi(\eta)$.

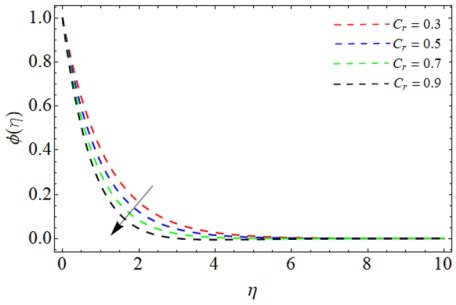

FIG. 16. Chemical reaction C_r vs $\phi(\eta)$.

A higher fluid velocity across the wedge surface is the result of buoyancy forces driving the flow.

Figures 9–14 show the influence of the Dufour number D_4, *Nb*, *Nt*, *Pr*, *Rd*, and Weissenberg number *Wi* on energy field $\theta(\eta)$, respectively. Figures 9–11 elucidate that the thermal profile develops with the rising impact of D_4, *Nb*, and *Nt*, respectively. In fact, D_4 is known as the energy flux due to the concentration difference and because it offers a coupled non-reversible progression. Hence, the change in D_4 enriches the energy curve $\theta(\eta)$ (Fig. 9). Figures 10 and 11 also show that the energy curve boosts with the rising impact of *Nb* and *Nt*. Physically, due to the internal collisions of fluid molecules, they generate heat, which causes advancement in fluid temperature $\theta(\eta)$(Figs. 10 and 11). Figures 12 and 13 expose

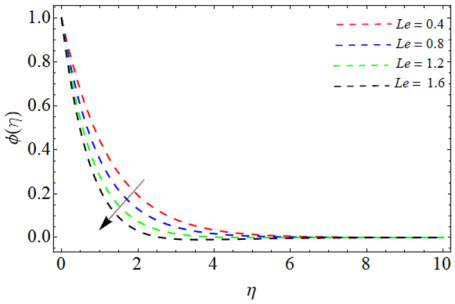

FIG. 17. Lewis number *Le* vs $\phi(\eta)$.

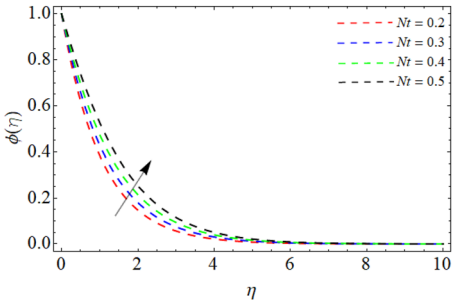

FIG. 18. Thermophoresis factor *Nt* vs $\phi(\eta)$.

that the energy cure of THNF declines with the variation in *Pr*, but enhances with the upshot *Rd*. Physically, fluid with the high Prandtl value has always less thermal diffusivity, and that's why, the fluid energy curve $\theta(\eta)$ falls off with the effect of *Pr* as publicized in Fig. 12. The upshot of thermal radiation parameter carries heat from the source to the fluid flow, which causes elevation in the energy curve $\theta(\eta)$ as offered in Fig. 13. Figure 14 reveals the outcome of an energy field $\theta(\eta)$. Physically, *Wi* is the ratio between fluid viscosity and elasticity. This physical fact explains why the thicknesses of the energy boundary layers increase as *Wi* increases since the energy curve boosts with the effect of *Wi* (Fig. 14). Figures 15 and 16 illustrate the impact of *Nb* and chemical reaction factor *Kr* on the concentration field, respectively. The impact of both parameters exposes that the mass profile $\phi(\eta)$ drops with the variation

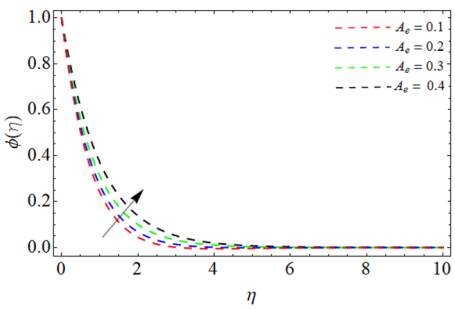

FIG. 19. Activation energy A_e vs $\phi(\eta)$.

TABLE II. Numerical outcomes for $f''(0)$, $-\theta'(0)$, and $-\phi'(0)$.

m	W_i	n	Pr	Nb	Nt	D_4	Sr	M	Le	B	Rd	$f''(0)$	$-\theta'(0)$	$-\phi'(0)$
0.3	0.2	0.4	3.0	0.2	0.2	0.1	0.1	0.1	0.5	1	1	2.272 80	0.526 82	0.475 32
0.6												2.285 42	0.527 93	0.475 73
0.8	0.2											2.272 63	0.526 41	0.475 28
	0.4											2.239 63	0.522 98	0.473 19
	0.6	0.4										2.272 82	0.526 26	0.475 02
		0.7										2.260 02	0.528 36	0.476 78
		1.1	3.0									2.272 73	0.526 82	0.475 24
			5.0									2.245 46	0.513 01	0.626 13
			7.0	0.2								2.272 29	0.526 38	0.475 87
				0.3								2.261 52	0.446 48	0.611 28
				0.2	0.2							2.272 85	0.526 27	0.475 28
					0.4							2.263 29	0.463 59	0.258 81
					0.2	0.1						2.272 88	0.526 92	0.475 36
						0.5						2.220 62	0.160 43	0.722 27
						0.1	0.1					2.272 81	0.526 21	0.475 18
							0.5					2.280 52	0.579 97	0.218 28
							0.1	0.1				2.372 90	0.526 36	0.475 91
								0.4				2.206 82	0.527 89	0.476 18
								0.1	0.5			2.272 13	0.526 90	0.475 89
									0.8			2.262 41	0.454 13	1.032 23
									0.5	1.0		2.272 36	0.526 37	0.475 35
										2.0		2.482 24	1.063 87	0.374 13
										1.0	1	2.272 60	0.526 17	0.475 23
											2	3.352 13	0.384 44	0.545 89

in Nb and Kr. Figures 17 and 18 highlight the impact of Le and Nt on the mass curve, respectively. The escalating values of Le diminish the concentration outline, whereas the variation in Nt augments the mass profile $\phi(\eta)$. Figure 19 displays the nature of activation energy A_e vs $\phi(\eta)$. Physically, the diffusion processes and the rate of reactions are impacted by the activation energy factor, and this eventually affects the concentration of fluids. Higher concentrations of fluid and material accumulation result from slower reactions or less diffusion caused by a higher activation energy.

Table II presents the numerical results for shearing stress $f''(0)$, Nusselt number, and $-\phi'(0)$. It has been pragmatic that the variation in wedge angle boosts the shearing stress and energy propagation rate, whereas the increment of Wi declines both the energy transfer rate and skin friction.

V. CONCLUSIONS

We have numerically reported the combined effect of wedge angle and melting energy transfer on the tangent hyperbolic MHD nanoliquid flow through a permeable wedge. The consequences of chemical reaction, Soret and Dufour, heat source/sink, and thermal radiation are also examined on the flow of THNF. The flow has been formulated in the form of PDEs, which are numerically calculated through the BVP4c. The numerical results of BVP4c are relatively compared to the published work for the validity purpose. The main conclusions are as follows:

- The fluid velocity significantly improves with the rising impact of the buoyancy forces.
- The impact of surface permeability factor K_p drops the fluid velocity.
- The flow velocity $f'(\eta)$ enhances with the increment of power law index n and magnetic factor M.
- The variation in the wedge angle boosts the shearing stress and energy propagation rate, whereas the increment of Wi declines both the energy transfer rate and skin friction.
- The fluid velocity augments with the impact of wedge angle term m, but diminishes against the variation in Weissenberg number Wi.
- The energy curve enriches with the rising impact of D_4, Nb, and Nt.
- The impact of Nb and chemical reaction factor drops with the variation in the mass profile $\phi(\eta)$.
- The energy cure of THNF declines with the variation in Pr, but enhances with the upshot Rd.
- The positive variation in the activation energy parameter elevates the mass diffusion rate of THNF.
- The rising values of Le diminish the concentration outline, whereas the variation in Nt augments the mass profile $\phi(\eta)$.

ACKNOWLEDGMENTS

The authors extend their appreciation to Taif University, Saudi Arabia, for supporting this work through project number (TU-DSPP-2024-94).

AUTHOR DECLARATIONS

Conflict of Interest

The authors have no conflicts to disclose.

Author Contributions

Taghreed A. Assiri: Resources (equal); Validation (equal); Visualization (equal); Writing – review & editing (equal). **Muhammad Bilal**: Conceptualization (equal); Writing – original draft (equal). **Emad E. Mahmoud**: Investigation (equal); Methodology (equal); Visualization (equal); Writing – review & editing (equal). **Aatif Ali**: Investigation (equal); Writing – original draft (equal). **Joshua Kiddy K. Asamoah**: Data curation (equal); Visualization (equal); Writing – review & editing (equal). **Adnan**: Data curation (equal); Formal analysis (equal); Resources (equal); Software (equal).

DATA AVAILABILITY

The data that support the findings of this study are available within the article.

REFERENCES

[1]N. T. Eldabe, M. Y. Abou-Zeid, O. H. El-Kalaawy, S. M. Moawad, and O. S. Ahmed, "Electromagnetic steady motion of Casson fluid with heat and mass transfer through porous medium past a shrinking surface," Therm. Sci. **25**(1 Part A), 257–265 (2021).

[2]S. Nandi and B. Kumbhakar, "Navier's slip effect on Carreau nanofluid flow past a convectively heated wedge in the presence of nonlinear thermal radiation and magnetic field," Int. Commun. Heat Mass Transfer **118**, 104813 (2020).

[3]Y. Dadhich, R. Jain, and S. Gyeltshen, "Insights of heat and mass transfer in magneto-mixed convective Sisko nanofluid over a wedge with viscous dissipation," Math. Probl. Eng. **2022**, 3091897 (n.d.).

[4]A. Tassaddiq, S. Khan, M. Bilal, T. Gul, S. Mukhtar, Z. Shah, and E. Bonyah, "Heat and mass transfer together with hybrid nanofluid flow over a rotating disk," AIP Adv. **10**(5), 055317 (2020).

[5]K. A. M. Alharbi, A. E. S. Ahmed, M. Ould Sidi, N. A. Ahammad, A. Mohamed, M. A. El-Shorbagy, M. Bilal, and R. Marzouki, "Computational valuation of Darcy ternary-hybrid nanofluid flow across an extending cylinder with induction effects," Micromachines **13**(4), 588 (2022).

[6]K. A. M. Alharbi, M. Bilal, R. Allogmany, and A. Ali, "The numerical study of nanofluid flow with energy and mass transfer over a stretching/shrinking wedge," Proc. Inst. Mech. Eng., Part E **237**(6), 2134–2143 (2023).

[7]T. A. Assiri, F. A. Aziz Elsebaee, A. M. Alqahtani, M. Bilal, A. Ali, and S. M. Eldin, "Numerical simulation of energy transfer in radiative hybrid nanofluids flow influenced by second-order chemical reaction and magnetic field," AIP Adv. **13**(3), 035020 (2023).

[8]M. Rahman, T. A. Assiri, S. Saifullah, M. A. Khan, and M. Sun, "Some new optical solitary waves solutions of a third order dispersive Schrödinger equation with Kerr nonlinearity using an efficient approach associated with Riccati equation," Opt. Quantum Electron. **56**(4), 1–13 (2024).

[9]G. Dharmaiah, F. Mebarek-Oudina, M. Sreenivasa Kumar, and K. Chandra Kala, "Nuclear reactor application on Jeffrey fluid flow with Falkner-Skan factor, Brownian and thermophoresis, non linear thermal radiation impacts past a wedge," J. Indian Chem. Soc. **100**(2), 100907 (2023).

[10]Z. I. Butt, I. Ahmad, M. Shoaib, H. Ilyas, and M. A. Z. Raja, "A novel design of inverse multiquadric radial basis neural networks to analyze MHD nanofluid boundary layer flow past a wedge embedded in a porous medium under the influence of radiation and viscous effects," Int. Commun. Heat Mass Transfer **140**, 106516 (2023).

[11]P. Rana, S. Gupta, and G. Gupta, "FEM computations and Taguchi optimization in nonlinear radiative MHD MWCNT-MgO/EG hybrid nanoliquid flow and heat transfer over a 3D wedge surface," Case Stud. Therm. Eng. **41**, 102639 (2023).

[12]B. Ali, R. A. Naqvi, A. Mariam, L. Ali, and O. M. Aldossary, "Finite element study for magnetohydrodynamic (MHD) tangent hyperbolic nanofluid flow over a faster/slower stretching wedge with activation energy," Mathematics **9**(1), 25 (2020).

[13]T. Kebede, E. Haile, G. Awgichew, and T. Waleligh, "Heat and mass transfer analysis in unsteady flow of tangent hyperbolic nanofluid over a moving wedge with buoyancy and dissipation effects," Heliyon **6**(4), e03776 (2020).

[14]U. Shahzad, M. Mushtaq, S. Farid, K. Jabeen, and R. M. A. Muntazir, "A Numerical Approach for an unsteady tangent hyperbolic nanofluid flow past a wedge in the presence of suction/injection," Math. Probl. Eng. **2021**, 1–15.

[15]S. Hussain, F. Ahmad, H. Ayed, M. Y. Malik, H. Waqas, M. M. Al-Sawalha, and S. Hussain, "Combined magnetic and porosity effects on flow of time-dependent tangent hyperbolic fluid with nanoparticles and motile gyrotactic microorganism past a wedge with second-order slip," Case Stud. Therm. Eng. **26**, 100962 (2021).

[16]I. S. Ud Din, I. Siddique, R. Ali, F. Jarad, S. Abdal, and S. Hussain, "On heat and flow characteristics of Carreau nanofluid and tangent hyperbolic nanofluid across a wedge with slip effects and bioconvection," Case Stud. Therm. Eng. **39**, 102390 (2022).

[17]A. U. Yahya, I. Siddique, N. Salamat, S. Abdal, and S. Hussain, "A numerical investigation for tangent hyperbolic hybrid nanofluid transportation across Riga wedge," Waves Random Complex Media (published online) (2022).

[18]K. A. M. Alharbi, M. Bilal, A. Ali, S. M. Eldin, A. Alburaikan, and H. A. E. W. Khalifa, "Significance of gyrotactic microorganisms on the MHD tangent hyperbolic nanofluid flow across an elastic slender surface: Numerical analysis," Nanotechnol. Rev. **12**(1), 20230106 (2023).

[19]A. Mahdy and A. J. Chamkha, "Unsteady MHD boundary layer flow of tangent hyperbolic two-phase nanofluid of moving stretched porous wedge," Int. J. Numer. Methods Heat Fluid Flow **28**(11), 2567–2580 (2018).

[20]S. Abdal, I. Siddique, A. S. Alshomrani, F. Jarad, I. S. Ud Din, and S. Afzal, "Significance of chemical reaction with activation energy for Riga wedge flow of tangent hyperbolic nanofluid in existence of heat source," Case Stud. Therm. Eng. **28**, 101542 (2021).

[21]H. Waqas, U. Farooq, M. M. Bhatti, and S. Hussain, "Magnetized bioconvection flow of Sutterby fluid characterized by the suspension of nanoparticles across a wedge with activation energy," J. Appl. Math. Mech. **101**(12), e202000349 (2021).

[22]L. Ali, B. Ali, X. Liu, T. Iqbal, R. M. Zulqarnain, and M. Javid, "A comparative study of unsteady MHD Falkner–Skan wedge flow for non-Newtonian nanofluids considering thermal radiation and activation energy," Chin. J. Phys. **77**, 1625–1638 (2022).

[23]M. Bilal, N. H. Hamad, S. A. AlQahtani, and P. Pathak, "Numerical simulation of nanofluid flow across a slender stretching Riga plate subjected to heat source and activation energy," Numer. Heat Transfer, Part B (published online) (2024).

[24]S. A. Alsallami, H. Zahir, T. Muhammad, A. U. Hayat, M. R. Khan, and A. Ali, "Numerical simulation of Marangoni Maxwell nanofluid flow with Arrhenius activation energy and entropy anatomization over a rotating disk," Waves Random Complex Media (published online) (2022).

[25]T. Sajid, M. K. Al Mesfer, W. Jamshed, M. R. Eid, M. Danish, K. Irshad, R. W. Ibrahim, S. Batool, S. M. El Din, and G. C. Altamirano, "Endo/exothermic chemical processes influences of tri-hybridity nanofluids flowing over wedge with convective boundary constraints and activation energy," Results Phys. **51**, 106676 (2023).

[26]H. A Othman, B. Ali, S. Jubair, M. Yahya Almusawa, and S. M. Aldin, "Numerical simulation of the nanofluid flow consists of gyrotactic microorganism and subject to activation energy across an inclined stretching cylinder," Sci. Rep. **13**(1), 7719 (2023).
[27]M. Ramzan, N. Shaheen, J. D. Chung, S. Kadry, Y. M. Chu, and F. Howari, "Impact of Newtonian heating and Fourier and Fick's laws on a magnetohydrodynamic dusty Casson nanofluid flow with variable heat source/sink over a stretching cylinder," Sci. Rep. **11**(1), 2357 (2021).
[28]B. Mahanthesh, K. Thriveni, and G. Lorenzini, "Significance of nonlinear Boussinesq approximation and non-uniform heat source/sink on nanoliquid flow with convective heat condition: Sensitivity analysis," Eur. Phys. J. Plus **136**, 418 (2021).
[29]Adnan, W. Abbas, N. M. Said, N. K. Mishra, Z. Mahmood, and M. Bilal, "Significance of coupled effects of resistive heating and perpendicular magnetic field on heat transfer process of mixed convective flow of ternary nanofluid," J. Therm. Anal. Calorim. **149**(2), 879–892 (2024).
[30]B. K. Sharma and R. Gandhi, "Combined effects of Joule heating and non-uniform heat source/sink on unsteady MHD mixed convective flow over a vertical stretching surface embedded in a Darcy-Forchheimer porous medium," Propul. Power Res. **11**(2), 276–292 (2022).
[31]A. W. Adnan, W. Abbas, A. M. Alqahtani, Z. Mahmood, S. A. Ould Beinane, and M. Bilal, "Numerical heat featuring in radiative convective ternary nanofluid under induced magnetic field and heat generating source," Int. J. Mod. Phys. B 2550044 (published online) (2024).
[32]T. Gul, J. U. Rahman, M. Bilal, A. Saeed, W. Alghamdi, S. Mukhtar, H. Alrabaiah, and E. Bonyah, "Viscous dissipated hybrid nanoliquid flow with Darcy–Forchheimer and forced convection over a moving thin needle," AIP Adv. **10**(10), 105308 (2020).
[33]W. Ibrahim, "Magnetohydrodynamics (MHD) flow of a tangent hyperbolic fluid with nanoparticles past a stretching sheet with second order slip and convective boundary condition," Results Phys. **7**, 3723–3731 (2017).
[34]S. M. Atif, S. Hussain, and M. Sagheer, "Effect of viscous dissipation and Joule heating on MHD radiative tangent hyperbolic nanofluid with convective and slip conditions," J. Braz. Soc. Mech. Sci. Eng. **41**, 189 (2019).
[35]M. Waqas, M. R. Almutiri, B. Yagoob, H. Ahmad, and M. Bilal, "Numerical analysis of MHD tangent hyperbolic nanofluid flow over a stretching surface subject to heat source/sink," Pramana **98**(1), 27 (2024).
[36]F. M. Allehiany, M. Bilal, W. F. Alfwzan, A. Ali, and S. M. Eldin, "Numerical solution for the electrically conducting hybrid nanofluid flow between two parallel rotating surfaces subject to thermal radiation," AIP Adv. **13**(7), 075005 (2023).
[37]F. A. A. Elsebaee, M. Bilal, S. R. Mahmoud, M. Balubaid, M. Shuaib, J. K. Asamoah, and A. Ali, "Motile micro-organism based trihybrid nanofluid flow with an application of magnetic effect across a slender stretching sheet: Numerical approach," AIP Adv. **13**(3), 035237 (2023).
[38]S. Sarkar and M. F. Endalew, "Effects of melting process on the hydromagnetic wedge flow of a Casson nanofluid in a porous medium," Boundary Value Probl. **2019**(1), 43–14.
[39]M. F. Endalew and S. Sarkar, "Numerical exploration of forced convection hydromagnetic hyperbolic tangent nanofluid flow over a permeable wedge with melting heat transfer," Sci. Rep. **13**(1), 3515 (2023).